Chapter 2

The Ring Imaging Cherenkov detector for CLAS12

To perform QCD measurements with flavor sensitivity, an efficient system to identify the hadrons in the final state is essential. This Chapter introduces the CLAS12 spectrometer focusing on the PID system and describes the Ring Imaging Cherenkov (RICH) detector. During this work, the author was involved in the assembly and commissioning of the second RICH module, in the efficiency study of the first module, and in the first physics analysis carried out using the RICH data. The first two of these activities are described in this Chapter.

2.1 The CLAS12 spectrometer at Jefferson Lab

The Thomas Jefferson National Accelerator Facility (JLab) is one of the most important laboratories dedicated to nuclear physics research thanks to the electron beam provided by the Continuous Electron Beams Accelerator Facility (CEBAF) and different apparatuses realized in four experimental halls. The JLab site is shown in Figure 2.1. The high intensity, highly polarized, 12 GeV electron beam permits to perform sophisticated measurements aiming to probe and possibly extend the Standard Model of particle physics via precise parity violation measurement, light dark matter and exotic particle searches, three-dimensional nucleon structure and parton dynamics investigation, exploiting the peculiarities of the four halls. A scheme of CEBAF is represented in Figure 2.2.

The experimental Hall B hosts the CEBAF Large Acceptance Spectrometer for operation at 12 GeV (CLAS12)[16], a spectrometer developed by an international collaboration of 48 institutions. CLAS12 is based on a dual-magnet system, constituted by a torus magnet (forward region) and a solenoid magnet (target region), and it is designed to provide efficient detection of charged and neutral particles over a large fraction of the solid

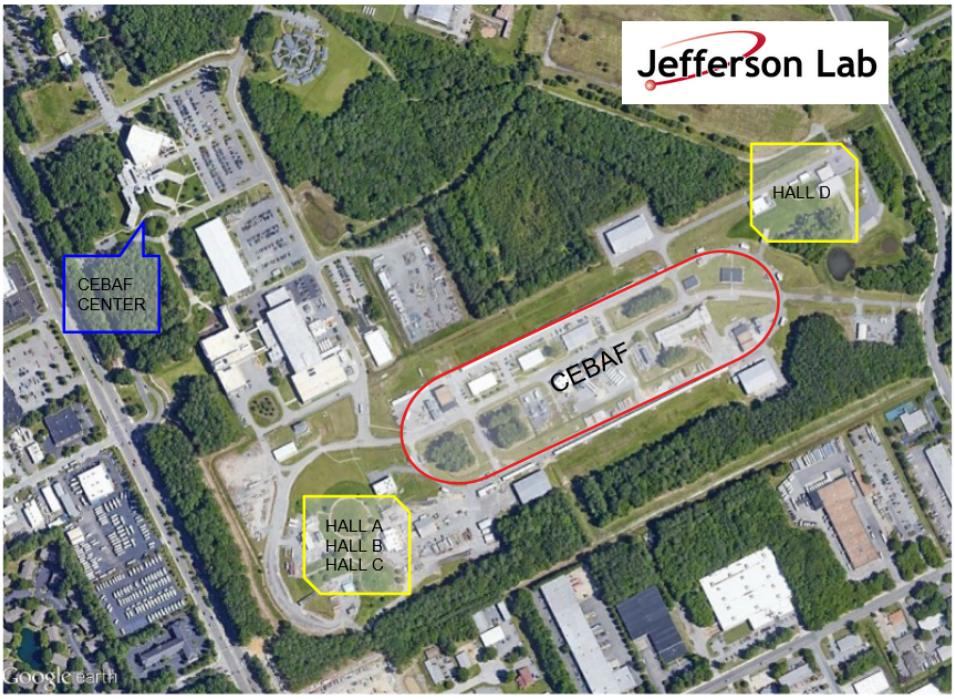

Figure 2.1: The JLab site

Figure 2.2: The CEBAF and experimental halls scheme

angle. The main goals of the CLAS12 physics program are:

- Nucleon structure studies using exclusive and semi-inclusive deep inelastic scattering processes by mapping the Generalized Parton Distributions (GPDs)[1] and Transverse-Momentum-Dependent (TMD)s;
- Precision measurement of structure functions and forward parton distribution at high x_B;
- Elastic and transition form factors at high momentum;
- Hadronization and color transparency;
- Hadron spectroscopy, studying heavy baryons and mesons with ordinary and exotic quantum numbers.

The magnets

The solenoid (Figure 2.3a) is made by self-shielded superconducting coils surrounding the beamline and used to generate a magnetic field primary in the beam direction. This design allows us to achieve the physics requirements of shielding the Moeller electron background, tracking particles with large angles, and providing a uniform field in the center to operate dynamically polarized proton and deuteron targets. The solenoid generates a 5 T field at its center at the maximum current.

The torus (Figure 2.3b) magnet comprises six identical superconducting coils, symmetrically arranged to obtain a toroidal field around the beamline. The geometrical coverage seen from the target is between 5° and 40°. The peak field is 3.58 T, while the field is zero at the center for reasons of symmetry.

2.1.1 The detector

CLAS12 can be divided into the Central Detector (CD) and the Forward Detector (FD).

The Central Detector

The CD is designed to detect particles covering the polar angle between 35° and 125° and almost the whole azimuthal angle. The CD is placed inside the solenoid magnet. The tracking and the measure of the momentum are provided by the Central Vertex Tracker (CVT), while the charged particle identification is entrusted to the Central Time-Of-Flight (CTOF). Moreover, the CD includes two neutron detectors, the Central Neutron Detector (CND)

[1] GPDs are a different way of accessing the nucleon structure. They are like tomographic slices of the form factors at a fixed value of the momentum fraction x_B

(a) CLAS12 solenoid **(b)** CLAS12 torus

Figure 2.3: The CLAS12 superconducting magnets.

and the Back Angle Neutron Detector (BAND). These detect neutrons with momentum up to 1.25 GeV and polar angle up to 175°.

The Forward Detector

The Forward Detector (FD) covers polar angles between 5° and 35°, with tracking, particle identification, and momentum measurement provided by different detectors. The FD structure is based on the torus magnet, so it is divided into six sectors that are identical in dimensions and almost identical in composition. All the sectors include three regions of Drift Chamber (DC) for tracking and two calorimeters, the Electromagnetic Calorimeter (EC) and Pre-shower Calorimeter (PCAL) for identification and kinematical reconstruction of electrons, photons, and neutrons. The only differences between sectors regard the Particle Identification (PID) components. Indeed, all six are equipped with a High Threshold Cherenkov Counter (HTCC) and a Forward Time-Of-Flight (FTOF), four sectors host a Low Threshold Cherenkov Counter (LTCC), and the other two a Ring Imaging Cherenkov (RICH) detector; more details about the PID are discussed in the following. Moreover, the FD includes the Forward Tagger (FT) to extend the capability of detecting electrons and photons at very forward polar angles between 2.5° and 4.5°, consisting of a calorimeter, a hodoscope, and a micro-strip gas tracker.

The FD Particle Identification

The PID, particularly the capability to distinguish charged hadrons and leptons, plays a crucial role in QCD studies with flavor sensitivity. Indeed, aiming to perform SIDIS measurements, the precise identification of the final states particles acquires great importance. The following detectors concur in the PID:

- The Forward Time-Of-Flight (FTOF) measures the time-of-flight of charged particles from the production target. The system is designed to reach an average time resolution of 80 ps to distinguish pions and kaons up to 3 GeV.

- The Low Threshold Cherenkov Counter (LTCC) is a Cherenkov counter that uses C_4F_{10} as a radiator; it allows the tag of the charged pions up to 3.5 GeV.

- The High Threshold Cherenkov Counter (HTCC) separates the electrons and positrons with momenta below 4.9 GeV from charged hadrons. It operates in dry CO_2 gas at 1 atm pressure.

- Two Ring Imaging Cherenkov (RICH) detectors were added (the first in 2018 and the second in 2022) in two opposite sectors to improve the identification of charged kaons in higher momentum range inaccessible with the FTOF and LTCC. They are based on the measurement of the Cherenkov angle of the photons emitted by the charged particle passing through an aerogel radiator, which, combined with the kinematic information, allows the separation of the hadron species.

A scheme of the RICH and LTCC positions is shown in Figure 2.4. The author was directly involved in the assembly of the second module of the RICH, in the efficiency studies of the first module, and in the first analysis of SIDIS based on the RICH kaon identification.

2.2 The CLAS12 Ring Imaging Cherenkov

In 2018, a first Ring Imaging Cherenkov (RICH) detector [37] was incorporated into the CLAS12 spectrometer at JLab. A RICH detector exploits the Cherenkov photons produced by a charged particle crossing a radiator with a speed greater than the speed of light in that medium to identify the velocity of the particle. This information, combined with the momentum measured by other detectors, allows to identify the mass of the particle. The Cherenkov effect is described by

$$\cos\theta_{Ch} = \frac{1}{\beta n(\lambda)} \tag{2.1}$$

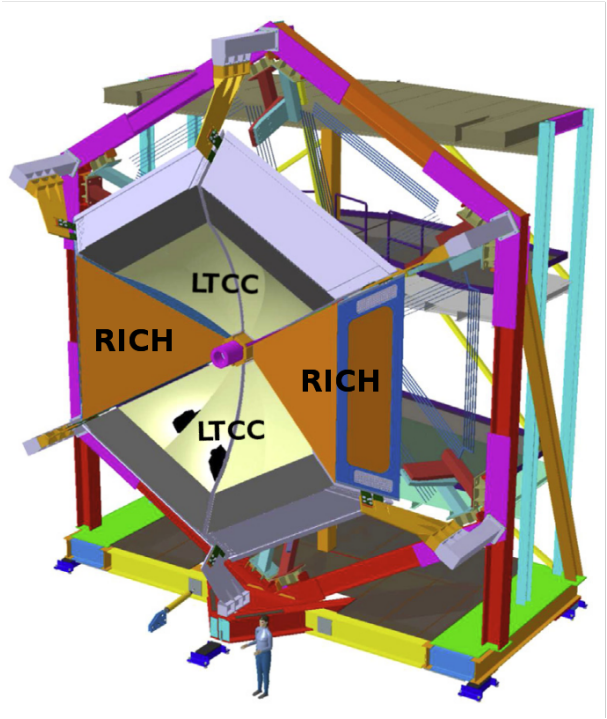

Figure 2.4: Scheme of the RICH and LTCC detectors position in CLAS12.

where θ_{Ch} is the opening angle of the photon from the particle trajectory, β is the particle's speed, and $n(\lambda)$ is the refractive index of the medium depending on the wavelength. After a gap region, the projection of the Cherenkov cone into an active surface is the so-called "ring", which has to be detected by light detectors operating in single-photon mode. A generic RICH functioning scheme is shown in Figure 2.5a. The CLAS12 RICH was explicitly designed to facilitate efficient kaon identification in the momentum range between 3 GeV/c and 8 GeV/c. Indeed, the original PID system based on FTOF, LTCC, and HTCC does not provide sufficient separation in this momentum range between kaons, pions, and protons for effective SIDIS studies on kaons. In 2022, a second module was installed, identical to the first. Figure 2.17b shows CLAS12 with the two RICH modules.

2.2.1 RICH design

According to the CLAS12 Monte Carlo studies, the kaons identification needs to achieve a rejection factor for pions in the order of $1:500$, corresponding to a separation of 4σ between pions and kaons. As shown in Figure 2.6, the only possible radiator is the silica aerogel, which has a very low macroscopic density and a refractive index between the gas and the liquids. The RICH has to fit inside the Forward Carriage of CLAS12, which imposes several

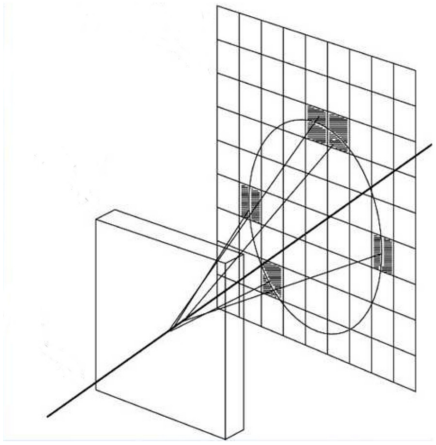

(a) Functioning scheme of a generic RICH detector

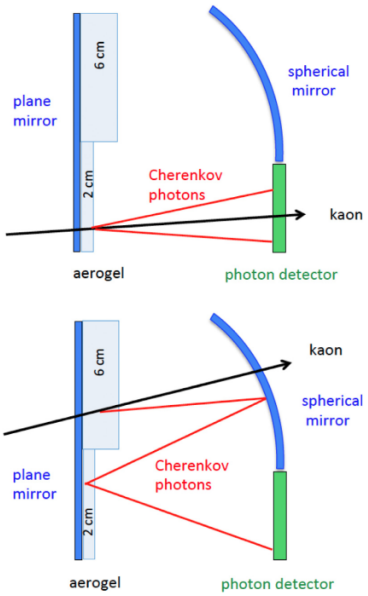

(b) On top direct imaging; on bottom imaging after one or more reflections on the mirrors.

Figure 2.5

constraints: a projective geometry, a limited depth of 1.2 m, and $\sim 4.5\,\mathrm{m}^2$ entrance windows. Based on the simulation, the RICH is designed to integrate the aerogel radiators, visible light photon detectors, and a focusing mirror system in a compact hybrid-optics design. The mirrors allow the reduction of the photon detector area to $\sim 1\,\mathrm{m}^2$, minimizing the cost and the impact on the downstream detectors. Depending on the polar angle of the incident particles, the photons can hit the photo-detection area directly, as shown in Figure 2.5b (top), or after multiple reflections with a second passage through the radiator, as shown in Figure 2.5b (bottom). To minimize the total material budget, the mechanical structure is made almost entirely of light composite materials, in particular carbon fiber. A complete detector scheme is shown in Figure 2.7.

2.2.2 The radiator

The radiator selected for the RICH was the silica aerogel, the only effective choice in the wanted $3 \div 8\,\mathrm{GeV}$ momentum range, as shown from the plot in Figure 2.6, where the expected Cherenkov angle for different hadrons is plotted as a function of the particle momentum. The aerogel is an amorphous solid network of SiO_2 nanosphere, and it has a very low macroscopic density and a refractive index intermediate between gas and liquid radiators. The

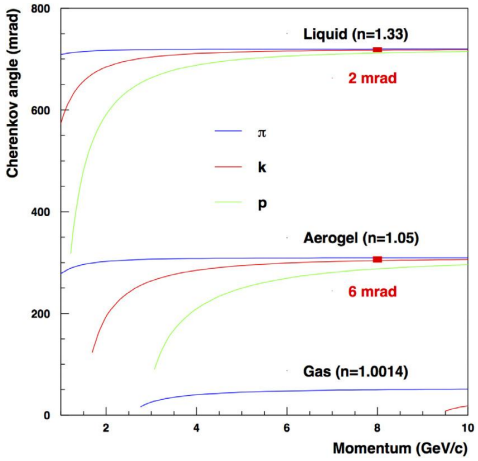

Figure 2.6: Expected Cherenkov angle for different hadron as a function of momentum for different radiators.

aerogel was produced by Budker and the Boreskov Institute of Nuclear Physics (Russia), which made all the 102 tiles of different shapes and thicknesses needed for each detector module. The tiles were assembled into two sections. The first, made of one layer of 2-cm-thick tiles, covers the region between the beam pipe up to the polar angle of 17.5°. The second region covers the polar angle between 17.5° and 26° and is made of two layers of 3-cm-thick tiles. Most tiles are squared $20 \times 20\,\mathrm{cm}^2$ bricks, but triangular, trapezoidal, and pentagonal shapes became necessary on the edges to cover the entire triangular entrance window. Each tile was tested [38] to determine the side length, thickness, and surface planarity. Also, the optical parameters were measured, particularly the refractive index at the reference wavelength of 400 nm and the light transmission as a function of the wavelength. Using the Hunt parametrization [39], the parameters of transparency A_0, clarity C, and scattering length at 400 nm Λ_S were extracted. From these measurements, the expected mean photon yield is 19 photoelectrons (p.e.) for the 2-cm-thick layer and 25 p.e. for the 6-cm-thick layer.

2.2.3 The mirror system

According to the simulation, the mirror system was designed to minimize the loss of photons and direct most of them to the photon detector. A drawing of the entire mirror system is shown in Figure 2.8.

The spherical mirror

The spherical mirror comprises ten sub-mirrors produced by the *Composite Mirror Applications* company [40]. It covers a total surface of $3.6\,\mathrm{m}^2$ and has a curvature radius of 2.7 m. This mirror is placed in front of the entrance

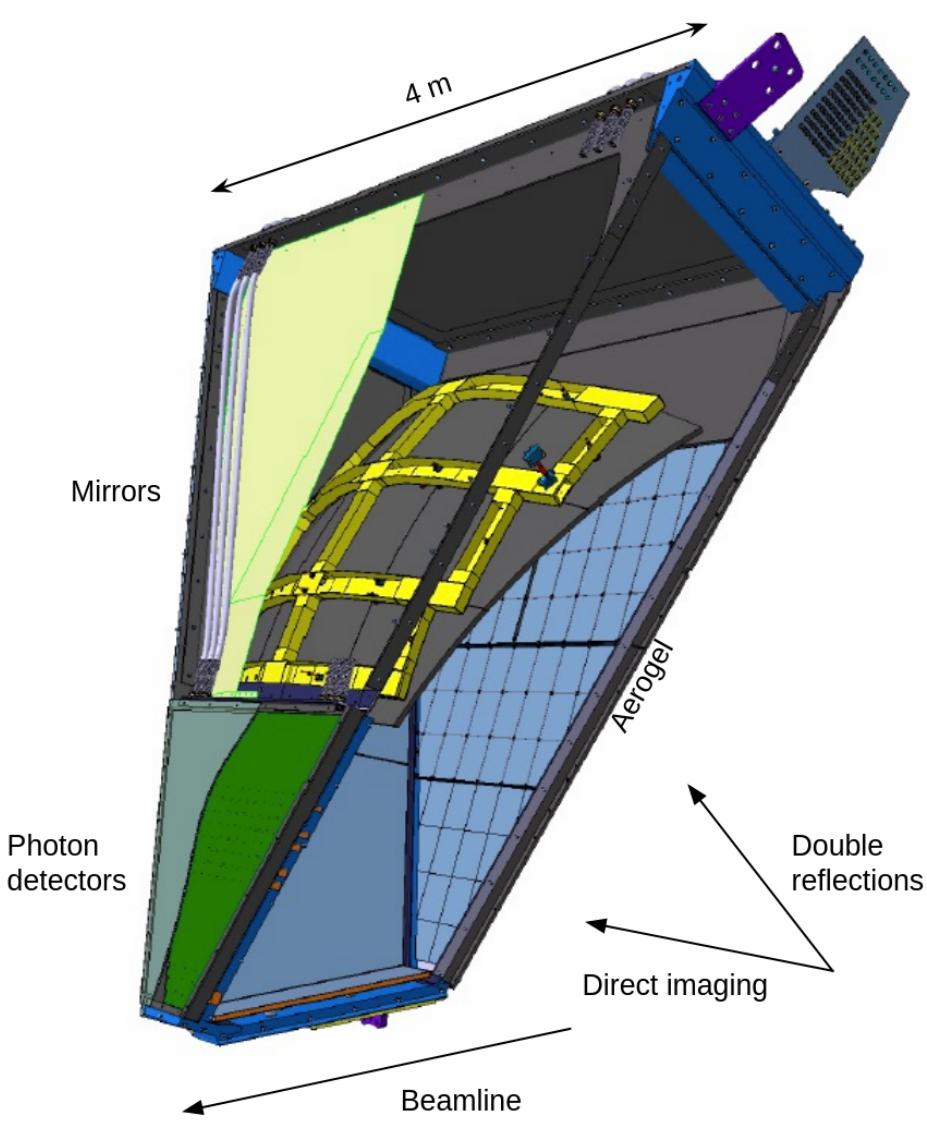

Figure 2.7: Sketch of the full RICH: the aerogel tiles, the structure supporting the spherical mirrors, and the photo-detection plane are indicated.

window to collect the photons produced by particles entering with a large polar angle. The accuracy of each sub-mirror spherical surface was quantified via the spot size measurement, illuminating the mirror with a point-like source and observing the size of the reflected spot with a CCD camera in its center. The size spot is quantified by D_0, the minimum diameter containing 90% of the reflected light, which is related to the angular resolution by

$$\sigma_\theta = \frac{D_0}{8R} \tag{2.2}$$

where R is the curvature radius. The mirror mechanical substrate is made by a sandwich of two carbon fiber layers with a honeycomb core that achieves a high rigidity and a low material budget of $0.01X_0$. The mirrors were coated with a reflective SiO_2 layer by the *Evaporated Coating* company [41]. The reflectivity of the mirrors is measured to be between 88% and 90% in the $300 - 700\,\text{nm}$ wavelength range of interest.

The planar mirrors

There are seven planar mirrors, two placed on each side of the detector, one on the bottom, and two on the front panel supporting the aerogel, covering a total surface of $6.5\,\text{m}^2$. They were produced by the *Media Lario* company [42], which is used to work for terrestrial telescope applications. The mirrors are made of two skins of glass glued on an aluminum honeycomb core; the front mirror skins are 0.7 mm thick to reduce the mirror material budget to $\sim 0.01X_0$ in the detector acceptance, while the lateral mirror skins have a more standard 1.6 mm thickness. The reflectivity of the planar mirrors has been measured to be greater than 90% in the $300 - 700\,\text{nm}$ range of wavelength and shows a maximum of about 95% at 400 nm.

2.2.4 The photon detector

The mirrors were designed to reduce the photo-detection area to $\sim 1\,\text{m}^2$, in the region close to the beamline where most of the particles are produced and with the most demanding high momenta concentration.

The photo-sensor

To make imaging possible, the photo-sensor has to work efficiently in the Single PhotoElectron (SPE) regime and be sensitive to visible light (to match the aerogel emission spectrum). Moreover, it must have the spatial resolution required to achieve the designed angular resolution, provide an active area with minimal dead space, and be insensitive to the low torus fringe field where the RICH readout is located (estimated to be no more than 3.5 G). The Hamamatsu flat-panel Multi-Anode Photomultiplier Tube (MAPMT) H8500, an 8×8 array of $6 \times 6\,\text{mm}^2$ pixels covering a $5 \times 5\,\text{cm}^2$ area, was

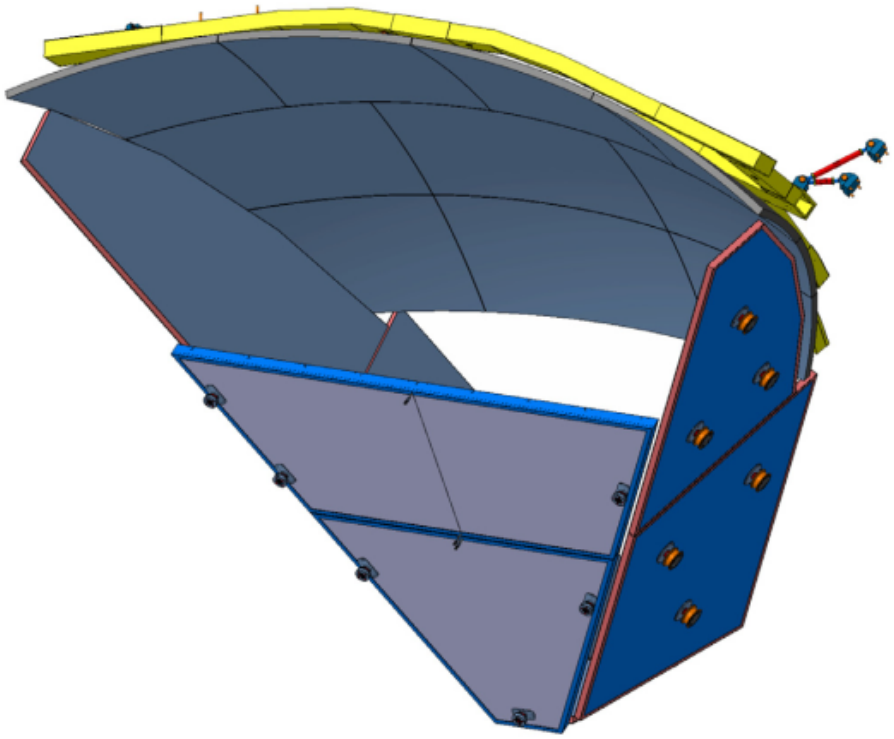

Figure 2.8: RICH mirror system draw. The spherical mirror has ten different spherical mirrors reflecting the light backward. Two mirrors upstream on the aerogel reflect the photons a second time in the direction of the MAPMTs, as shown in figure 2.5b. To minimize the photon loss, two planar mirrors on each side and one on the bottom surround the rest of the RICH module.

initially selected as photo-sensor. However, it was not designed for the SPE regime. Just after the start of the RICH construction, Hamamatsu released the H12700 MAPMT, which has the same layout and an optimized dynode structure for SPE. The first RICH combines 80 H8500 and 311 H12700 for a total of 391 photo-sensors, while the second module is fully equipped with H12700. This configuration results in 25024 pixels covering the $\sim 1\,\mathrm{m}^2$ trapezoidal active area of each RICH module. Figure 2.9a, shows a view of the MAPMTs side of the electronic panel.

The readout electronics

The front-end electronics is organized in compact modules called tiles serving two or three MAPMTs. The tile scheme is shown in Figure 2.10. The front-end electronics is intended to ensure a 100% discrimination efficiency at $\frac{1}{3}$ of the average photoelectron signal level, 1 to 4 gain spread compensation, and time resolution of the order of 1 ns to distinguish direct from reflected hits. Additionally, it has to sustain a 20 kHz trigger rate with 8 µs latency and negligible dead time. A stack of three different boards makes each readout unit:

- The adapter board provides the electrical connectivity of the sensors with the readout, preserving the light and gas tightness when the electronic panel is mounted in the detector. It also distributes the power to the MAPMTs, with a nominal bias of $-1000\,\mathrm{V}$.

- The ASIC board mounts two or three Multi-Anode ReadOut Chip (MAROC) chips, a 64-channel microcircuit dedicated to the processing of MAPMTs signals.

- The FPGA board hosts a Xilinx7 FPGA chip responsible for configuring and reading the MAROC chips, distributing the trigger, and interfacing with the DAQ system.

To connect the readout system, three kinds of cable are in use for each tile: the low-voltage cables to power the FPGA and the digitization chain, the high-voltage cable to power the MAPMTs, and the optical fiber for the communication between the FPGA and the DAQ system. The electronic panel was completed with a grounding grid, which attenuates the electronic noise, and the cooling system, based on a flow of compressed dry air that allows to maintain the temperature of the FPGA below the critical value of 75 °C. A picture of the full readout electronics of the RICH is reported in Figure 2.9b.

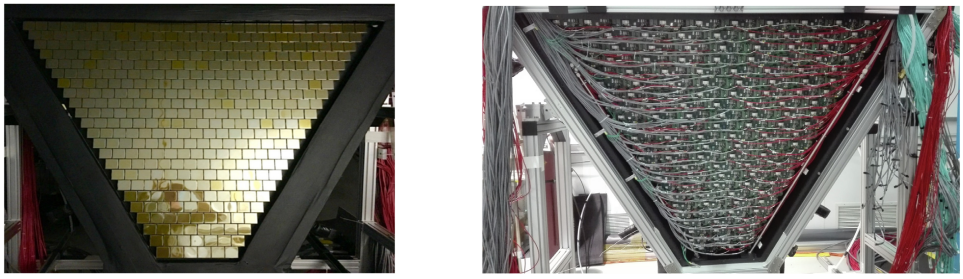

(a) MAPMTs side **(b)** Front-end electronic side

Figure 2.9: The RICH electronic panel.

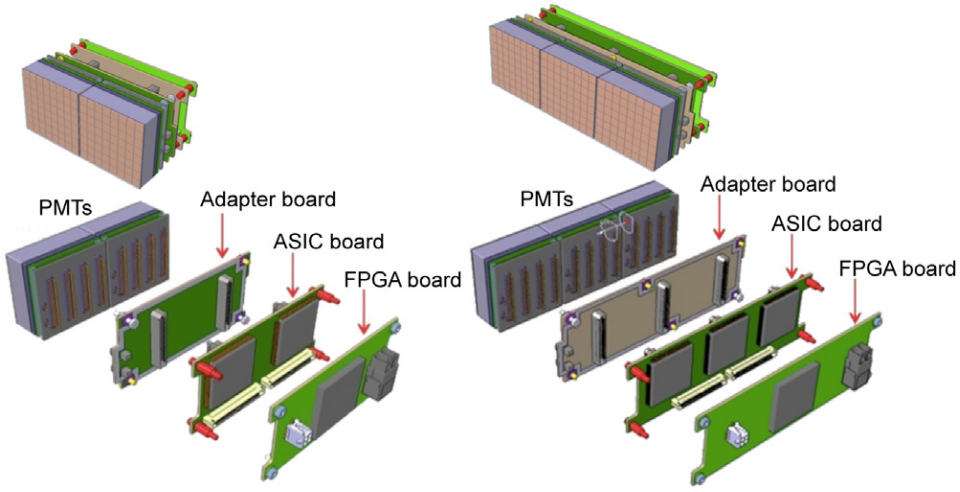

Figure 2.10: Scheme of the front-end electronic tiles serving two (left) or three (right) MAPMTs.

2.3 The assembly and commissioning of the second module of the RICH

In the spring of 2022, the author was directly involved in the assembling the second module of the RICH, in particular focusing on the electronic panel mounting and the installation of the detector inside the CLAS12 experiment. The assembling process before the installation was performed inside a clean room at JLab, and each subsystem was ~~installed in~~ the detector structure after the completion of the relative characterization tests. The expert of mechanics from INFN Frascati took care of the assembly of the RICH vessel (see Figure 2.13a), which has to sustain the entire detector structure. The spherical mirrors were characterized and then mounted in their support structure inside the vessel, while the planar mirrors were directly mounted on the vessel's walls (Figure 2.13d). The characterization includes measurements of the reflectivity in several points and of the point-like reflected spot size (Figure 2.12). The then spherical sub-mirrors were aligned using a point-like source and converging the reflected spots on the same point (Figure 2.13c). The hydrophobic aerogel was purged with a flux of nitrogen and mounted on the inner side of the frontal panel, in the section with (Figure 2.11a) and without (Figure 2.13b) mirrors. The INFN Ferrara team, including the author, worked mainly on the electronic panel, starting from ~~placing~~ the adapter boards on the inner side and connecting them with the ASIC boards on the other side (Figure 2.13e). Then, they added the FPGA boards to the ASIC boards and cabled all the 138 tiles (Figure 2.13f). After completing this step, the 391 MAPMTs were put in place by members of the Ferrara team, JLab and Duquesne University. All the readout units were connected to the power and DAQ system and tested (Figure 2.14). Under the supervision of the Frascati and Ferrara experts, the electronic panel was moved into the RICH vessel and tested again to ensure all the readout units worked correctly.

The last step was to place the frontal panel with the aerogel layer into the detector; the picture in Figure 2.11b was taken during this operation. This operation was particularly critical ~~since~~ the aerogel ~~was~~ placed on its supports ~~and can~~ be never turned face down. A CCD camera and a small portable light were placed inside the detector to check if any problem occurred during the moving phase. The completed RICH was tested for light leaks, which can cause problems for SPE, and gas leaks because the inner humidity needs to be minimized to maintain the aerogel properties. At the beginning of June 2022, the RICH was moved into Hall B (Figure 2.15), about 1 km from the clean room, using a truck with a special trolley. The assembly and transportation were made with the detector in a horizontal position; in Hall B, it was rotated vertically, with the short side on the bottom and the large on top. Then, it was rotated clockwise along the axis that passes through the

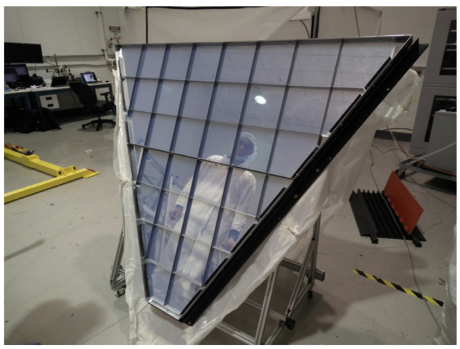

(a) The 2-cm-thick section of the aerogel mounted on the two frontal mirrors.

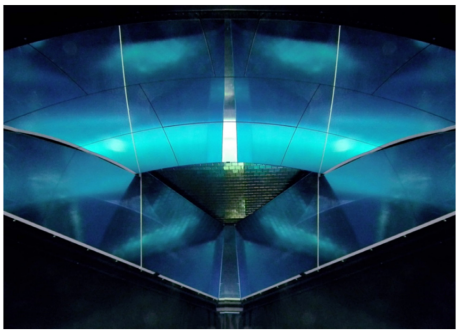

(b) Inside the RICH detector, the mirror system is seen from the entrance panel. From the top, clockwise, there are the ten spherical sub-mirrors, the two right mirrors, the bottom mirror, and the two left mirrors. At the center, the MAPMTs are visible.

Figure 2.11

(a) Reflectivity measurement apparatus.

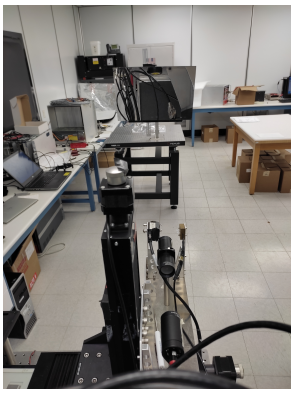

(b) Point-like reflected spot size measurement station.

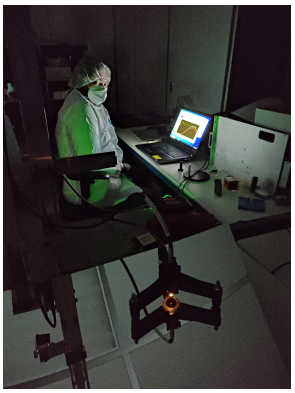

(c) The author during the measurement.

Figure 2.12

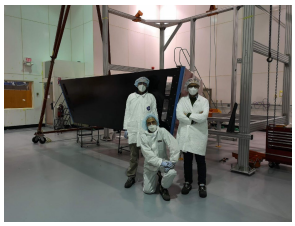

(a) RICH vessel

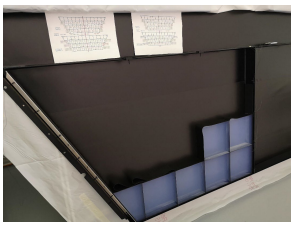

(b) Aerogel preparation

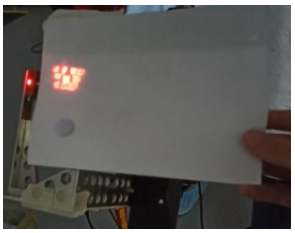

(c) Spherical mirror alignment

(d) Latera mirror assembly

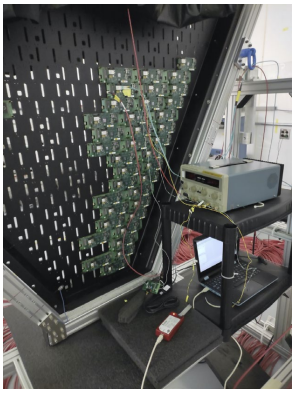

(e) Electronic Panel assembly and testing

(f) Electronic Panel cabling

Figure 2.13

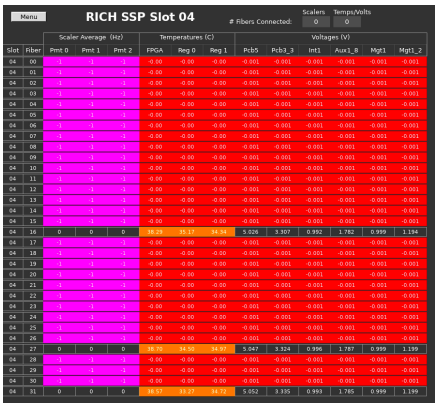

(a) Screenshot from the CLAS12 Slow Control system, which regulates the detector's power supply, during the first turning on of the full electronic panel.

(b) Termocamera picture of the electronic boards taken during the first functionality tests.

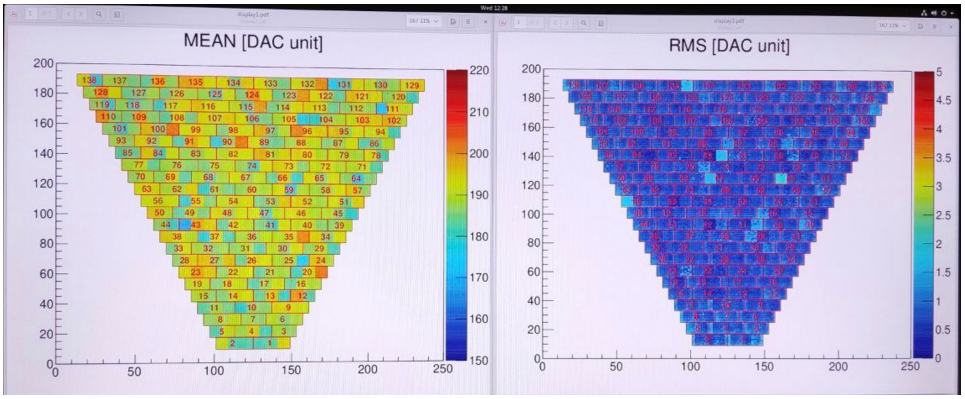

(c) Screenshot of the scaler plots taken during the first tests.

Figure 2.14

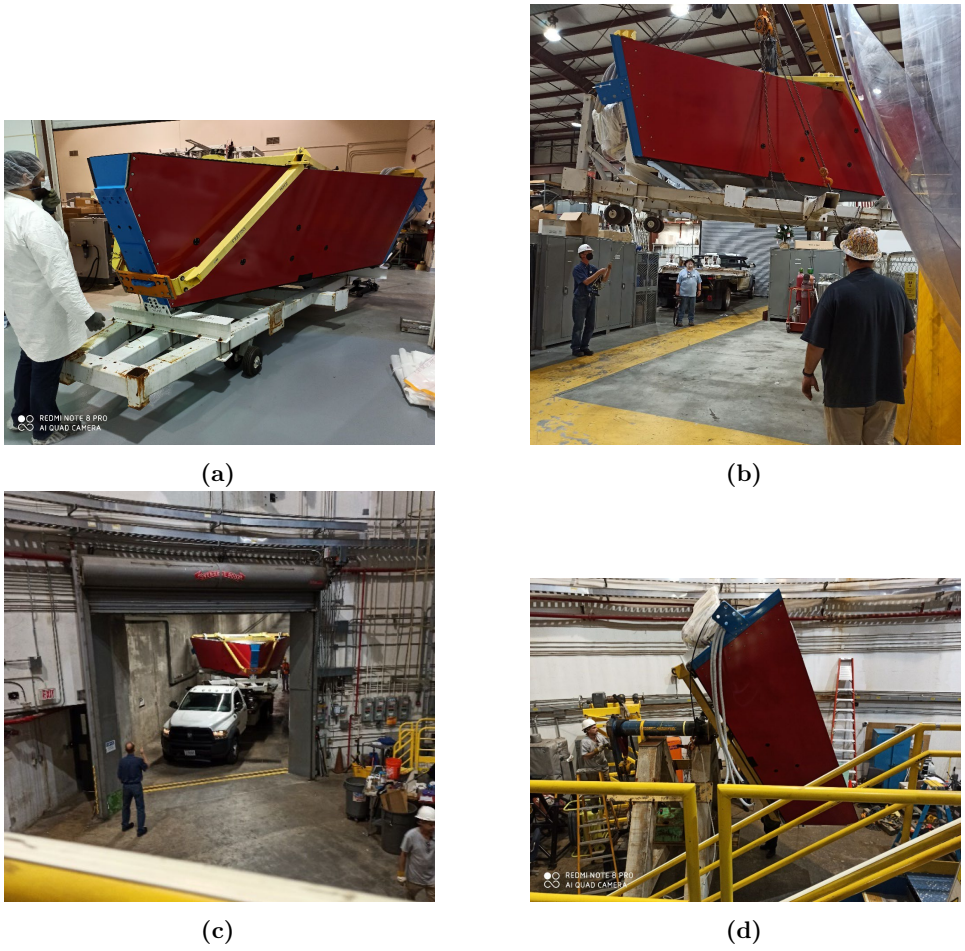

(a) **(b)**

(c) **(d)**

Figure 2.15: Moving of the RICH from the clean room to Hall B.

detector barycenter to place it in the final orientation with the short side on the right, close to the beamline, and the large side on the left. Finally, the RICH was raised to take its place inside the CLAS12 spectrometer. Since the moving phase was another critical step in the installation, the internal CCD camera was used to check again that no problem occurred to the aerogel. Figure 2.16 shows a picture taken inside the RICH after the installation.

Finally, the author was directly involved in cabling the RICH to the infrastructure of the CLAS12 experiment (Figure 2.17a). The picture of the complete array of RICH and LTCC modules of CLAS12 after the second RICH module installation is reported in Figure 2.17b. The RICH was included in the CLAS12 DAQ chain, and all the calibration and control procedures were extended from the first module. The first signals from the two modules are reported in Figures 2.17c and 2.17d.

Figure 2.16: View of the aerogel inside the RICH after its installation in Hall B.

(a) Cabling the RICH

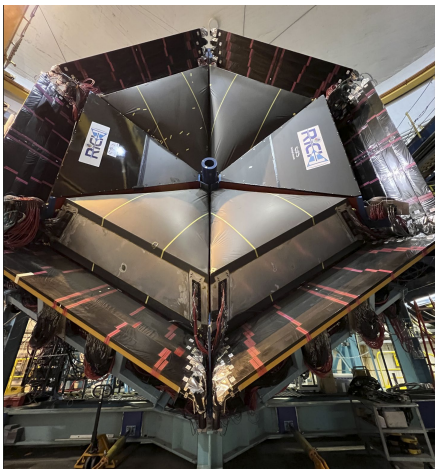

(b) Section of CLAS12 after installing the two modules of the Ring Imaging Cherenkov detector.

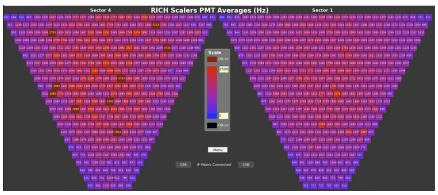

(c) First scaler map of the two modules.

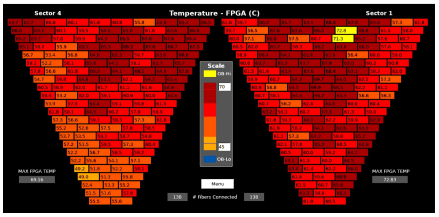

(d) First temperature map of the two modules.

Figure 2.17

2.4 RICH performance

The main goal of the RICH was to enhance the kaon identification and improve the pion rejection. As a consequence, the first study on the detector ~~effectiveness was performed~~ to evaluate the percentage of correctly identified pions and the percentage of pions misidentified as kaon, which was not a negligible number using the standard PID of CLAS12. The purity of the sample provided by the RICH can be ~~carried out~~ by comparing the missing mass of final states like eH^+X selected using the PID of CLAS12 (without the RICH) or the PID provided by the RICH. This study does not evaluate the detector's efficiency but its capability to provide a kaon sample with small pion contamination. It defines a sort of preliminary ~~fiducial cut~~ for identifying kaon based on the RICH variables that will be used in the analysis described in the next Chapter.

2.4.1 Data sample

The analysis was performed on a control sample containing data of the scattering of the 10.2 GeV electron beam off the Hydrogen target. The selection criteria applied are similar to the ones used in the SIDIS analysis described in Chapter 3 but less refined. The preliminary selection is based on the request that the electron was a trigger particle, its momentum was greater than 1.5 GeV, and that the reduced χ^2_{track}/NDF of the hadron track is less than 8. To study the RICH performance in the design working range, the hadron momentum was selected to be in the momentum range from 3 to 8 GeV. Aiming to evaluate the RICH performances and compare them with CLAS12 PID without the RICH, an additional request was that both the RICH and CLAS12 event builder (which still does not include the RICH) ~~identify the hadron~~. The sample that survived these cuts consists of $\sim 5.1 \times 10^6$ events.

Currently, the range of the hadron polar angle is partially limited because the alignment of part of the spherical sub-mirrors in the reconstruction code has yet to be finalized. The polar angle covers values up to $\sim 15°$. The distribution of the polar angle and momentum of the hadron sample used for the analysis is shown in Figure 2.18.

Two ~~cuts~~ were applied to the detector-related variables to obtain a clean sample of kaons using the RICH. The first is the request ~~that the detector detects~~ at least three photons so that the ring can be well-defined. This selection criterium cuts $\sim 18.7\%$ of the events in the sample. The second requirement is based on a specific RICH variable that can be used to evaluate the reliability of the identification. A likelihood ratio with respect to an ideal model corresponding to the measurement provides a χ^2-like estimator of the goodness of the hypothesis. The likelihood ratio is computed for any possible ~~identification~~, and the ~~flavor~~ minimizing the χ^2 selects the identification

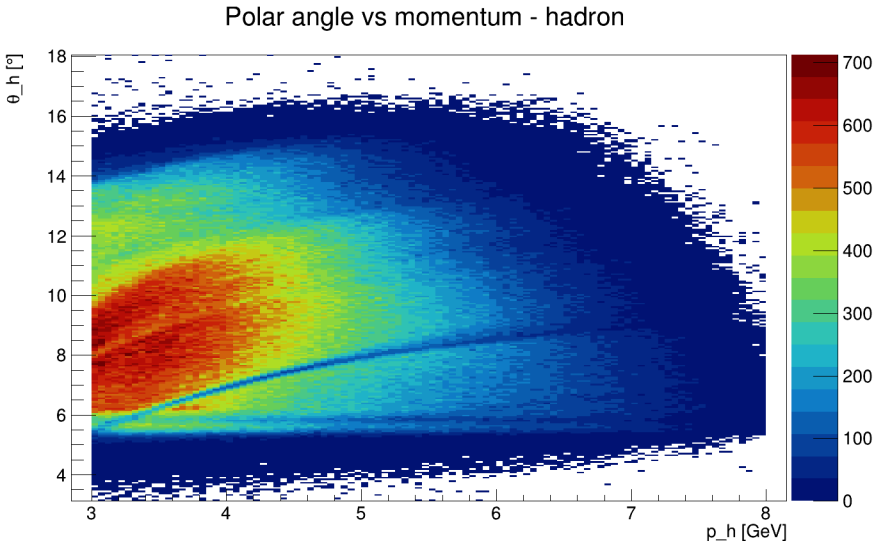

Figure 2.18: Polar angle and momentum of the hadron used for the study on the pion contamination of the kaon sample.

provided by the reconstruction software. Its value is defined by

$$\chi^2 \sim -2\log\lambda = 2(\overline{N} - N) + \sum_{i=1}^{N}\left[\frac{(\overline{\theta} - \theta_i)^2}{\sigma_\theta}\right] + \left[\frac{(\overline{t}(\theta) - t_i)^2}{\sigma_t}\right] \qquad (2.3)$$

where $\overline{N}, \overline{\theta}$, and $\overline{t}$ are the expected number ~~of photons~~, Cherenkov angle, and time of the photons, while N, θ_i, and t_i are the corresponding measured quantities. This variable provides an estimation of how much the identification is ~~good.~~ It ~~can exist in a~~ case in which the likelihoods of two different ~~identifications~~ are both ~~very good. In that case~~, the minimization of the likelihood is not enough to decide ~~if there is a better identification between the two hypotheses~~. ~~Then~~, an estimation of the goodness and unicity of identification can be ~~done~~ using the quantity defined as:

$$RQ = 1 - \frac{\lambda_{best}}{\lambda_{second\_best}}. \qquad (2.4)$$

If $RQ \to 0$, the identification tends to be ~~random~~ because the likelihoods for the two better hypotheses are very similar. If $RQ \to 1$, the best likelihood is ~~very small compared to the second best~~, then the identification is more reliable. There is a correlation between the likelihood ratio and the RQ, as it is shown in Figure 2.19. The number of events having a high likelihood ratio, more than 9, is very limited: checking it was less than 0.1%. Instead, the events with a low likelihood ratio and low RQ are not negligible. The distribution of the RQ quantity for the hadron sample used in this study is

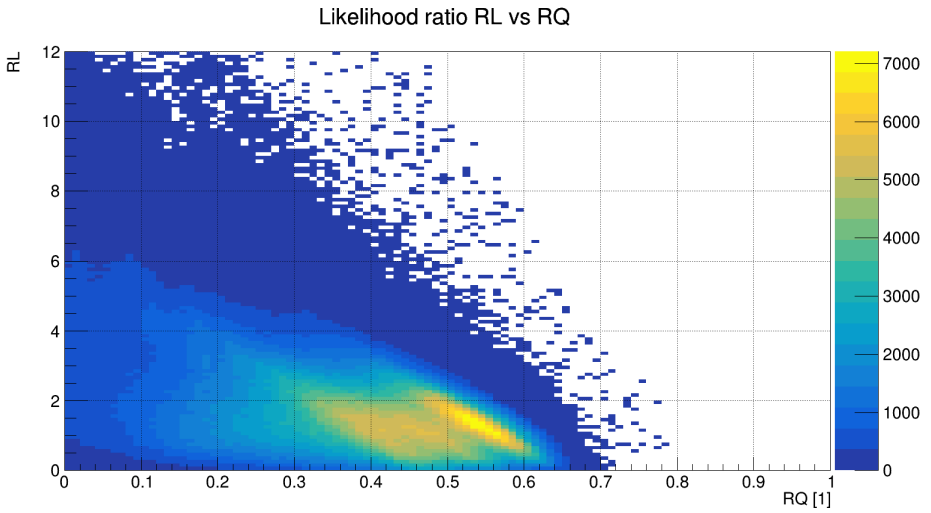

Figure 2.19: Distribution of the likelihood ratio and the RQ variables in the sample used for the RICH performance study.

shown in Figure 2.20. The kaon sample purity was evaluated by applying two different conditions on the RQ variable: ~~an empty~~ selection or the request of a value larger than 0.1. The last requirement reduced the available statistics of $\sim 7\%$. Combining the two requirements on the RICH variables, the events remained are 77.9% of which passed the non-RICH related cuts, constituting a sample of $\sim 4 \times 10^6$.

2.4.2 Analysis

The neutron peak at the missing mass of 0.94 GeV was used to evaluate the kaon sample purity and the pion identification efficiency. Indeed, the exclusive final state $e\pi^+ n$ is allowed, while the state $eK^+ n$ is forbidden for strangeness conservation. As a consequence, in the missing mass plot of events with a candidate kaon, the neutron peak should not be present, while it is expected in case the selected events include a pion.

A first qualitative idea of the RICH performance in cleaning the kaon sample is provided by the plots in Figure 2.21 and Figure 2.22, showing the missing mass of $e\pi^+X$ and eK^+X selected using the CLAS12 PID or the RICH PID. For eK^+X candidates, the neutron peak is evident using the CLAS12 PID, while it is strongly reduced using the RICH PID. In the $e\pi^+X$ plot, the number of events is larger using the RICH instead of the CLAS12 PID: this is because a part of the hadrons recognized by CLAS12 as kaons are actually pions, and the RICH correctly identified them. For the same reason, the statistic of the eK^+X sample selected by the RICH is lower than that of the sample identified by CLAS12.

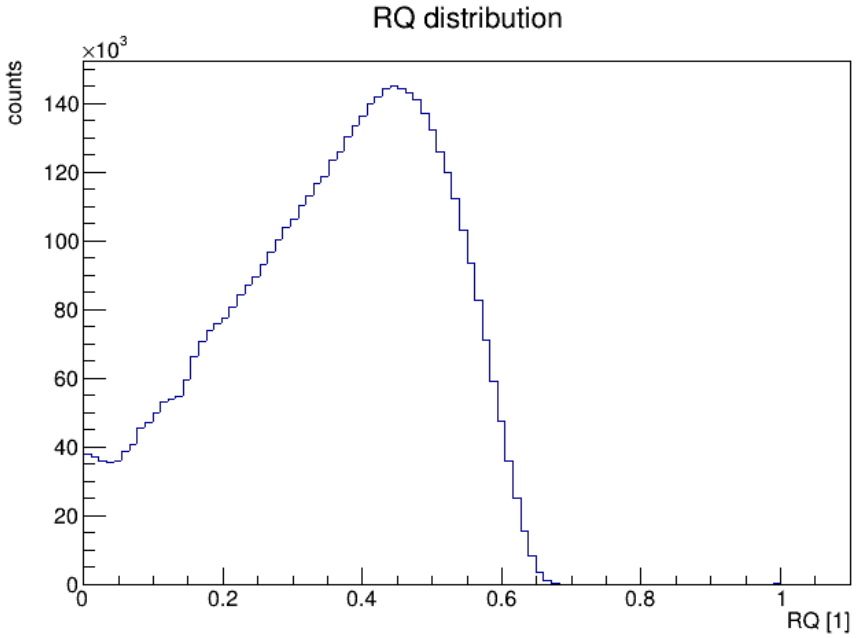

Figure 2.20: Distribution of the RQ variable for the hadron sample used in the RICH performance evaluation.

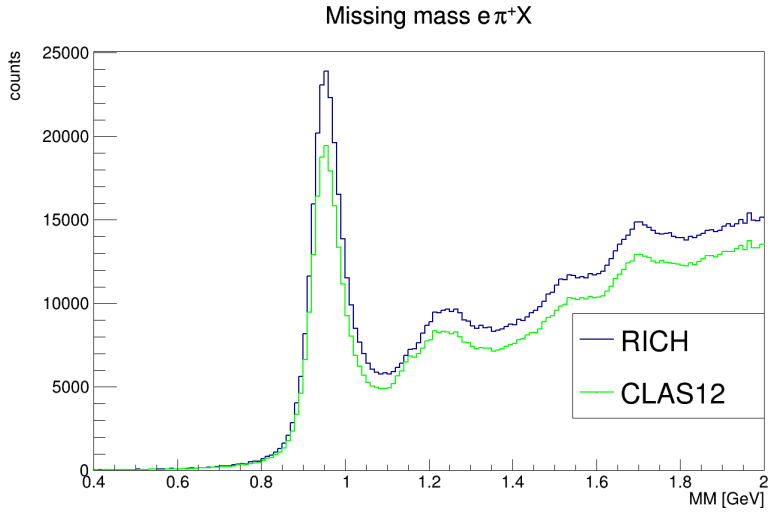

Figure 2.21: Missing mass of final state $e\pi^+X$ as identified by CLAS12 PID (green) or RICH PID (blue). The peak at 0.94 GeV signals the exclusive $e\pi^+n$ final state. The total number of events selected by CLAS12 is less than that selected by RICH because the first misidentified part of the hadrons as if they were kaons.

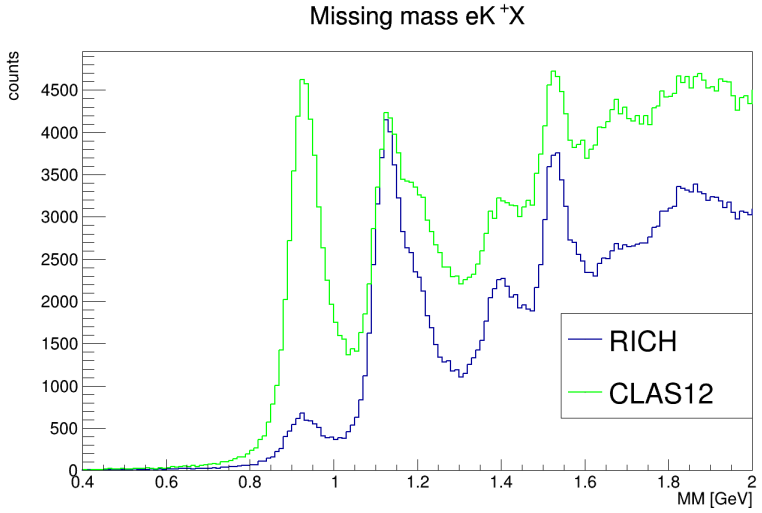

Figure 2.22: Missing mass of final state eK^+X as identified by CLAS12 PID (green) or RICH PID (blue). The clear reduction of the neutron peak at 0.94 GeV shows that the number of exclusives state $e\pi^+n$ decreases using the RICH; this corresponds to a lower number of pions misidentified as kaon, being forbidden the exclusive final state eK^+n. The total number of events selected by CLAS12 is more than that selected by RICH because the first misidentified part of the hadrons as if they were kaons.

The missing mass of the eK^+X sample defined by the RICH permits us also to show the capability of the RQ variable of removing ~~part~~ of the misidentification, as shown by the clear reduction of the neutron peak in Figure 2.23.

For a quantitative evaluation of the kaon sample purity, it was decided to extract the number of neutrons associated with the peak at 0.94 GeV and to define the pion identification efficiency ($\eta_{\pi\to\pi}$) as

$$\eta_{\pi\to\pi} = \frac{\text{Number of exclusive neutrons in } e\pi^+X \text{ events}}{\text{Number of exclusive neutrons in } (e\pi^+X + eK^+X + epX) \text{ events}} \tag{2.5}$$

and the percentage of pion misidentified as kaon ($\eta_{\pi\to K}$) as

$$\eta_{\pi\to K} = \frac{\text{Number of exclusive neutrons in } eK^+X \text{ events}}{\text{Number of exclusive neutrons in } (e\pi^+X + eK^+X + epX) \text{ events}} \tag{2.6}$$

having evaluated that the number of exclusive neutrons in the epX final state is small but not negligible.

To estimate the number of neutrons, the missing mass plots were fitted using a Gaussian function for the neutron peak, a ~~Gaussian~~ for the Δ^0 peak, two ~~Breit-Wigner~~ distributions for the Λ^0 and Σ^0, and one or more Gaussian and Breit-Wigner for other secondary plots. To describe the SIDIS

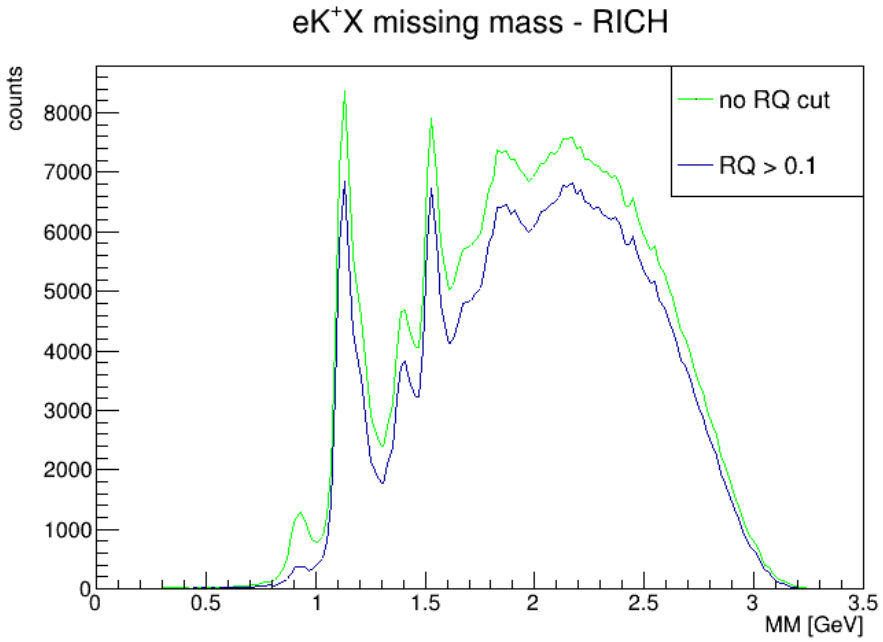

Figure 2.23: Missing mass of final state eK^+X identified by the RICH in case of applying the cut on RQ (blue) or not (green). The reduction of the neutron peak at 0.94 GeV provides the qualitative idea of the RQ cut effectiveness.

background shape, a Weibull-like distribution was used:

$$bkg_{Weib}(x; p_0, p_1, p_2) = p_0 x^{p1-1} \left(-\frac{x}{p_2}\right)^{p_1} \tag{2.7}$$

where x is the missing mass and p_0, p_1, and p_2 are parameters of the background. Three examples of fit for the pion, kaon, and proton cases are shown in Figures 2.24, 2.25, and 2.26. They show the missing mass of the samples in the ~~full~~ $3 \div 8$ GeV momentum range without the cut on RQ, for particle identified by the RICH. The same fit was applied to the analogous plots provided by the CLAS12 PID. The number of neutrons is estimated as the integral in $(\mu - 3\sigma, \mu + 3\sigma)$ region of the Gaussian associated with the neutron peak at 0.94 GeV. The reported error is the statistical uncertainty obtained as the count's square root. The missing mass plots obtained applying also the requirement $RQ > 0.1$ are shown in Figures 2.27, 2.28, and 2.29. Table 2.1 reports the number of neutrons obtained. As can be expected, ~~they show~~ a ~~-~~reduction in the total statistics and ~~that the number of pions misidentified as kaon is strongly reduced.~~ A counterintuitive phenomenon is that the pions ~~misidentified as protons~~ ~~in the RICH~~ are less ~~reduced than the corresponding misidentified as kaons~~. A possible explanation is that the likelihood used in the reconstruction software ~~depends on~~ the difference between the number of photons expected and measured. Because ~~the RICH usually detects few~~

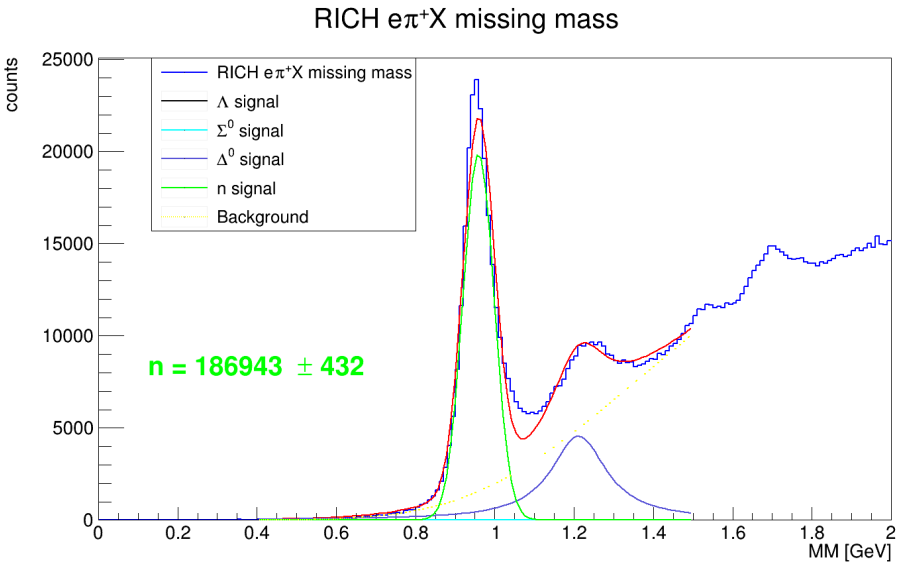

Figure 2.24: Fit of the missing mass plot of $e\pi^+X$ states selected by the RICH using the Weibull-like background. The green number is the quantity of neutrons estimated to be included in the peak, associated with the statistical error. In the pion case, the distributions associated with Λ and Σ^0 are fixed to zero.

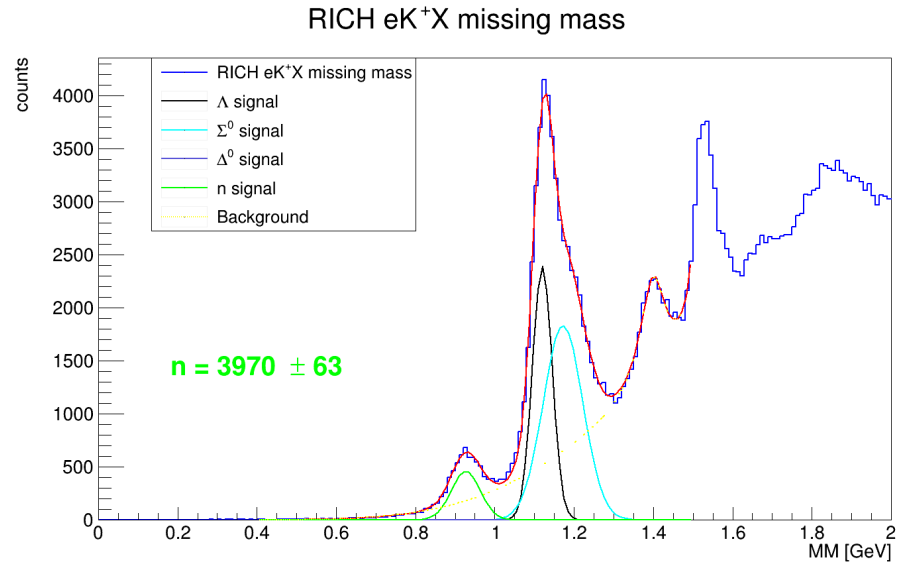

Figure 2.25: Fit of the missing mass plot of eK^+X states selected by the RICH using the Weibull-like background. The green number is the quantity of neutrons estimated to be included in the peak, associated with the statistical error. In the kaon case, the distribution associated with Δ^0 is fixed to zero.

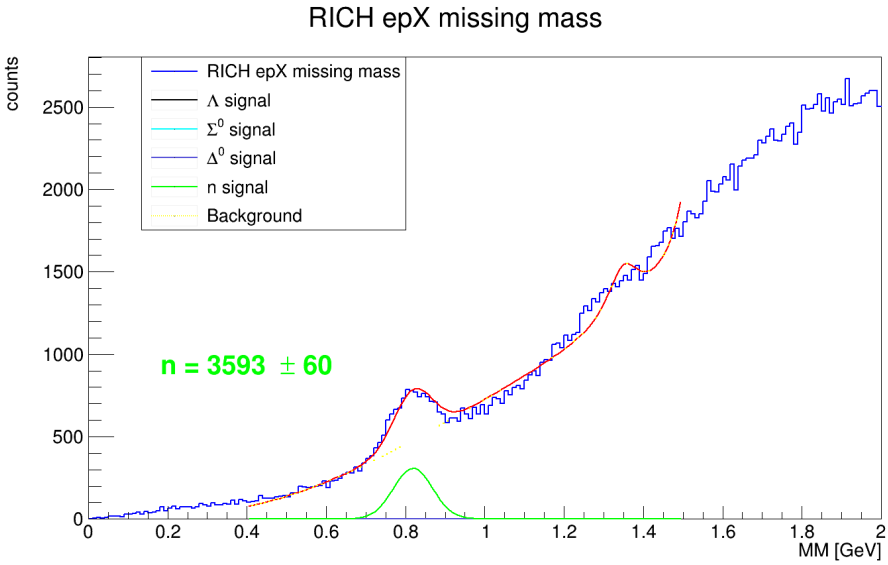

Figure 2.26: Fit of the missing mass plot of $e\pi X$ states selected by the RICH using the Weibull-like background. In the proton case, the neutron peak results particularly shifted with respect to the real masses 0.94 GeV because of the misidentification of pion and the wrong mass assignation. The green number is the quantity of neutrons estimated to be included in the peak, associated with the statistical error. In the proton case, the distributions associated with Λ, Σ^0, and Δ^0 are fixed to zero because the SIDIS background distribution is enough to describe the shape of the plot.

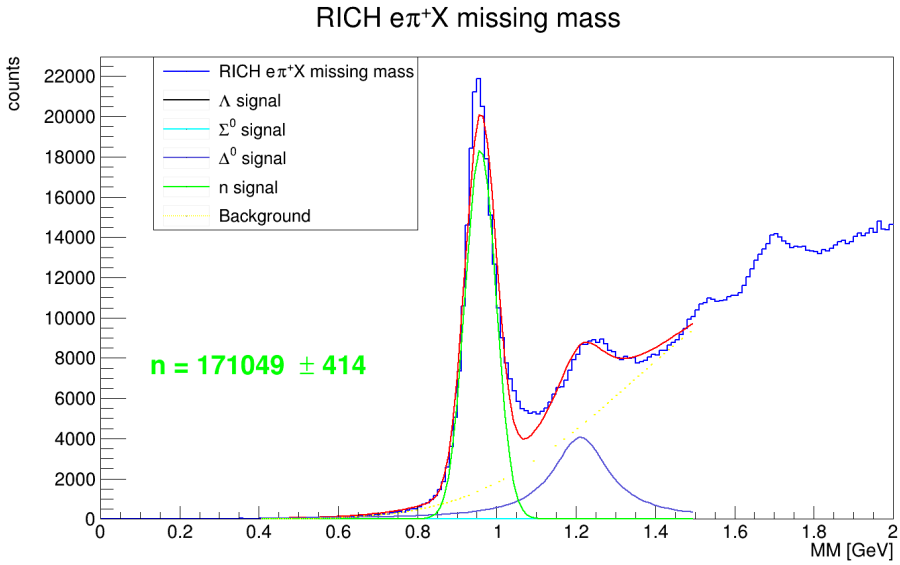

Figure 2.27: Fit of the missing mass plot of $e\pi^+X$ states selected by the RICH and applying the cut $RQ > 0.1$. The Weibull-like background was used. The green number is the quantity of neutrons estimated to be included in the peak, associated with the statistical error. In the pion case, the distributions associated with Λ and Σ^0 are fixed to zero.

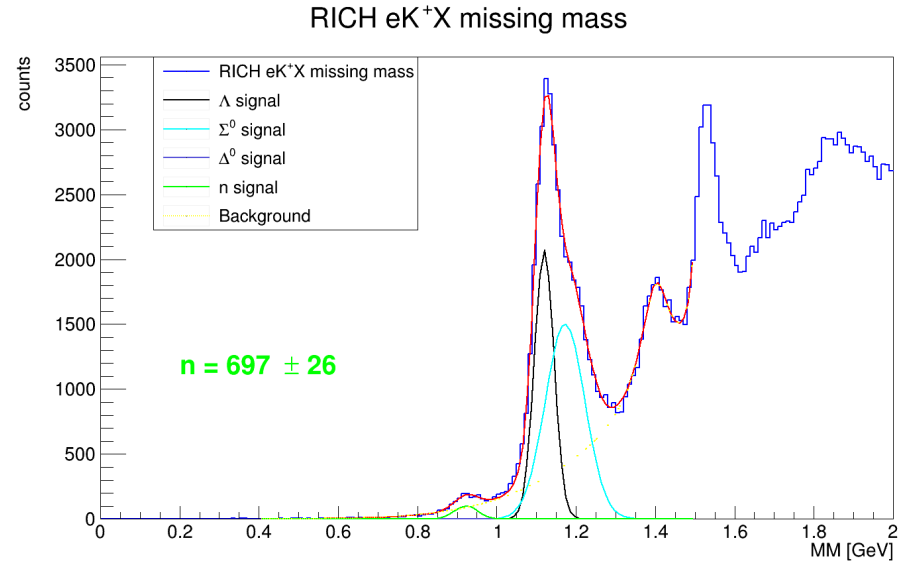

Figure 2.28: Fit of the missing mass plot of eK^+X states selected by the RICH and applying the cut $RQ > 0.1$. The Weibull-like background was used. The green number is the quantity of neutrons estimated to be included in the peak, associated with the statistical error. In the kaon case, the distribution associated with Δ^0 is fixed to zero.

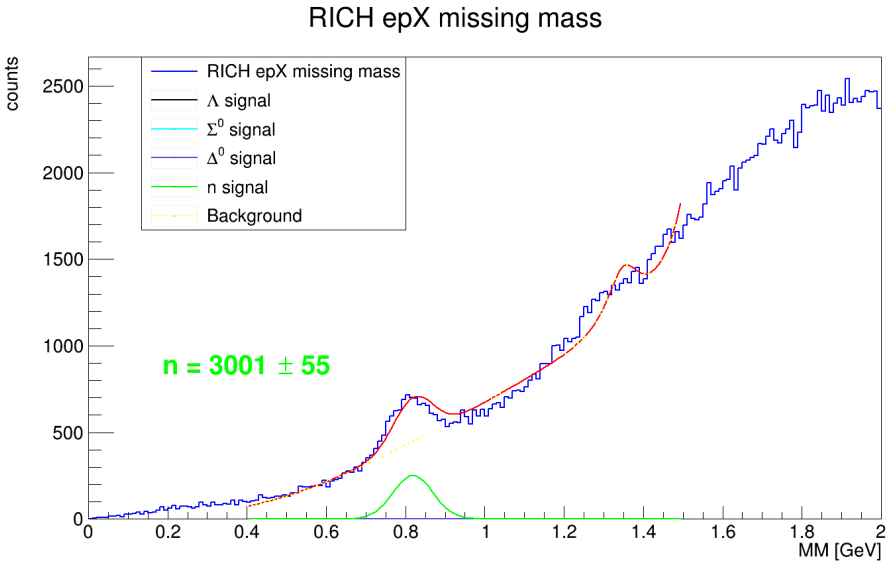

Figure 2.29: Fit of the missing mass plot of $e\pi X$ states selected by the RICH and applying the cut $RQ > 0.1$. The Weibull-like background was used. In the proton case, the neutron peak results particularly shifted with respect to the real masses 0.94 GeV because of the misidentification of pion and the wrong mass assignation. The green number is the quantity of neutrons estimated to be included in the peak, associated with the statistical error. In the proton case, the distributions associated with Λ, Σ^0, and Δ^0 are fixed to zero because the SIDIS background distribution is enough to describe the shape of the plot.

Final state	RQ cut	Number of neutrons
$e\pi^+X$	No	186943 ± 432
	Yes	171049 ± 414
eK^+X	No	3970 ± 63
	Yes	697 ± 26
epX	No	3593 ± 60
	Yes	3001 ± 55
Total	No	194506 ± 441
	Yes	174747 ± 418

Table 2.1: Recap of the number of neutrons extracted from the peak at 0.94 GeV in the missing mass plot.

~~photons, it can cause some distorting effects~~. The ~~further~~ studies needed to confirm this idea are beyond the aim of this analysis, which was to evaluate the purity of the kaon sample provided by the RICH.

In this study, data were binned in the hadron momentum p_H inside the detector's working range: $(3,4),(4,5),(5,6),(6,8)$. An analogous study showing a possible dependence from the polar angle of the hadron was postponed after the completion of the alignment of the spherical sub-mirrors, which will extend the range up to 26°. In this way, the photon yield can increase for particles currently on the edge of the phase space, making the identification more reliable.

2.4.3 Results

Providing a clean kaon sample

From design specification, the RICH is expected to provide a rejection factor of the pion in the kaon sample around 1 : 500 [37]. ~~By deriving~~ the mean percentage of misidentification in the total momentum range without the RQ cut from Table 2.1, ~~it~~ is

$$\eta^{RICH}_{\pi\to K}(3\,\text{GeV} < p_H < 8\,\text{GeV}) = (2.0 \pm 0.1)\% \tag{2.8}$$

where the error is the statistical uncertainty propagated to the result. ~~Clearly,~~ this result is not ~~comparable with~~ the expected performance. By applying the RQ cut the values became

$$\eta^{RICH}_{\pi\to K}(3\,\text{GeV} < p_H < 8\,\text{GeV}) = (0.4 \pm 0.1)\% \tag{2.9}$$

which is ~~closer~~ to the necessary performance to identify a clean kaon sample. ~~Then the RQ cut, combined with the cuts on the minimum number of photons and on the track reduced χ^2,~~ permits the achievement of a pion rejection factor comparable with the detector's expected performance of 0.2%. These

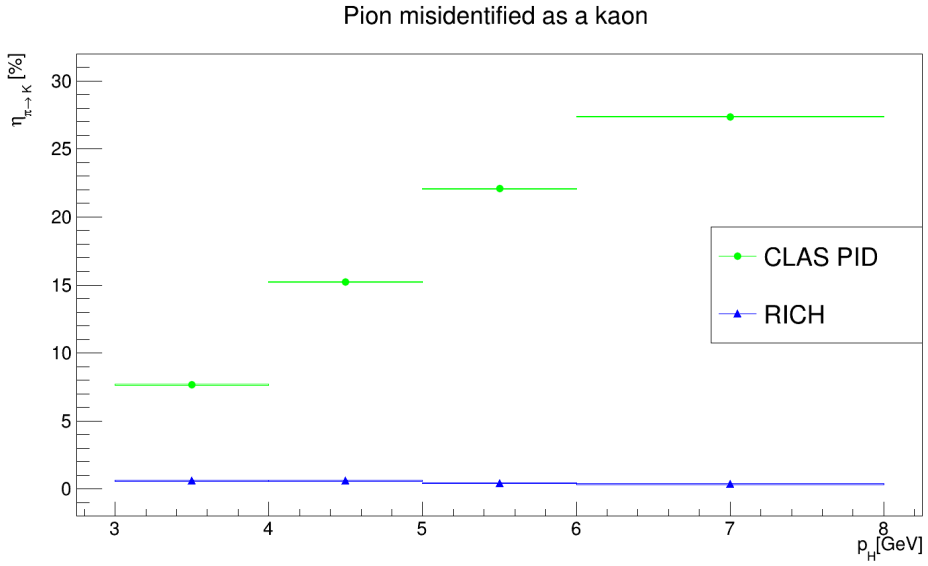

Figure 2.30: Percentage of pion misidentified as a kaon expressed as a function of the hadron momentum, applying the *RQ* cut. Because the error bars on the y-axis are smaller than the markers, the uncertainty was represented as a square centered on the graph point.

selection criteria constitute a sort of preliminary ~~fiducial cuts~~ of the RICH for kaon identification. Analyzing the same events using the CLAS12 PID (without the RICH), the mean misidentification is

$$\eta_{\pi\to K}^{CLAS12}(3\,\text{GeV} < p_H < 8\,\text{GeV}) = (19.6 \pm 0.6)\%. \tag{2.10}$$

This huge value can be explained because the CLAS12 PID was not originally designed to distinguish efficiently high-momentum hadrons, and corroborates the decision of the CLAS collaboration to install the RICH detector. The percentage is obviously independent of the *RQ* cut, applying which the misidentification becomes $(18.9 \pm 0.6)\%$, as it was expected from the fact that the cut is not related to the CLAS12 PID.

The comparison of the pions misidentification as kaon provided by the RICH and the CLAS12 PID as a function of the hadron momentum is shown in Figure 2.30. It shows that the $\eta_{\pi\to K}$ for the RICH is small and substantially the same for all the momentum bins, while it grows rapidly for the CLAS12 PID.

Pion contamination in kaon sample

The existence of a non-zero percentage of pions misidentified as kaons implies that there is some contamination ~~by~~ pions in the kaon sample. In particular, in the analyzed phase space, the pion statistic is expected to be significantly

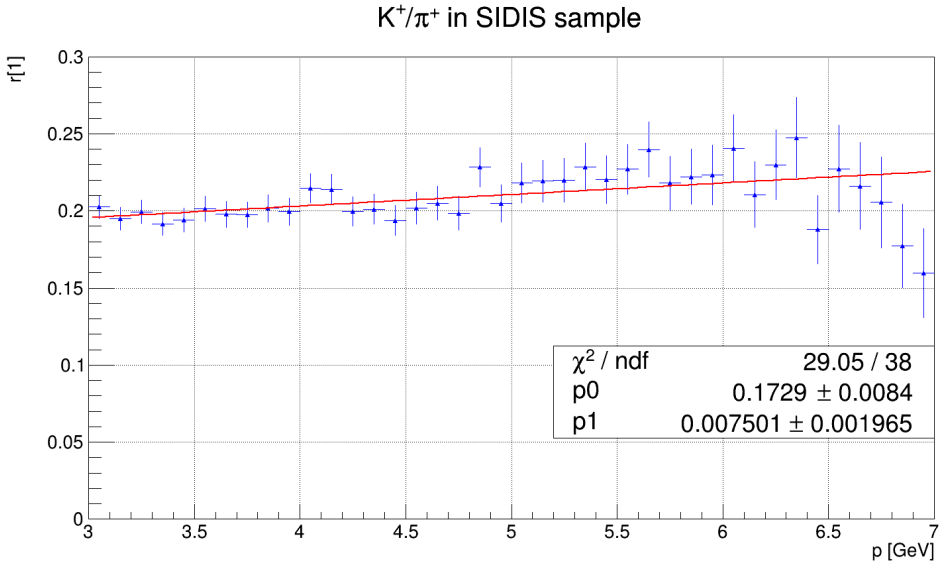

Figure 2.31: Ratio between the kaon and pion distributions as a function of the hadron momentum.

larger than the kaon statistic. The total contamination ~~could not be~~ negligible and introduces systematic effects on kaon SIDIS measurements.

To evaluate the contamination, the ratio between kaon and pion ~~statistics~~ was studied. It is shown in Figure 2.31 as a function of the hadron momentum (the low-statistic bins visible were excluded). The plot was fitted using a linear function to describe the trend of the ratio as a function of the momentum. The function was used to define the pion contamination in the kaon sample by multiplying it by the probability of misidentification $\eta_{\pi\to K}(p)$. The contamination as a function of the hadron momentum is shown in Figure 2.32. It was fitted using a linear function, to quantify the ~~trend and make it available for the study of systematic uncertainty introduced by the contamination described in Chapter 3 in measurements of kaon SIDIS~~.

Figure 2.33 shows the ratio between pion and kaon samples as a function of the hadron polar angle (the low-statistic bins were excluded). It shows a slow decrease before $\theta \simeq 12°$, then the decrease accelerates. Because, as shown in Figure 2.18, most of the hadrons have a polar angle between 5° and 12 degree and the kaon sample purity was not yet studied as a function of the hadron polar angle, the dependence of contamination from the polar angle was neglected.

Percentage of well-identified pion

The study provided also an estimation of the percentage of pions correctly identified with respect to the number of identifications, that applying the

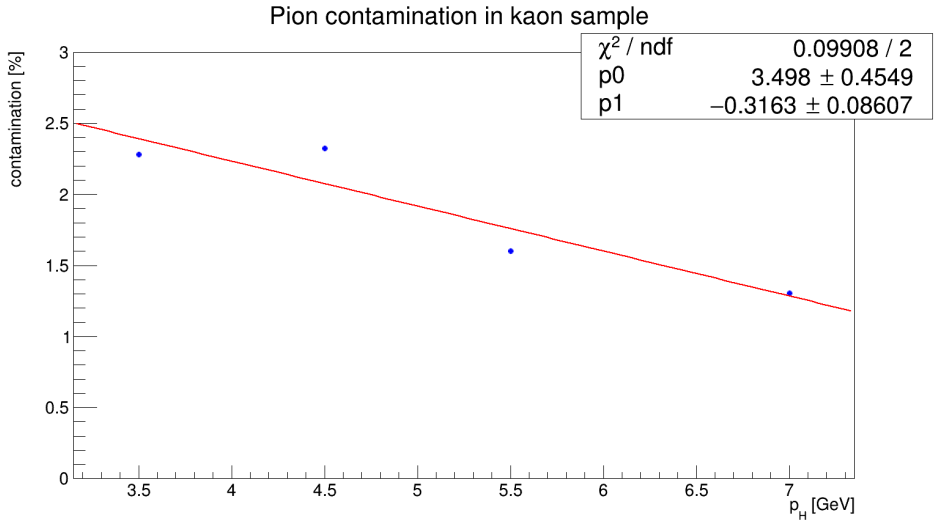

Figure 2.32: Contamination of kaon in the pion sample as a function of hadron momentum.

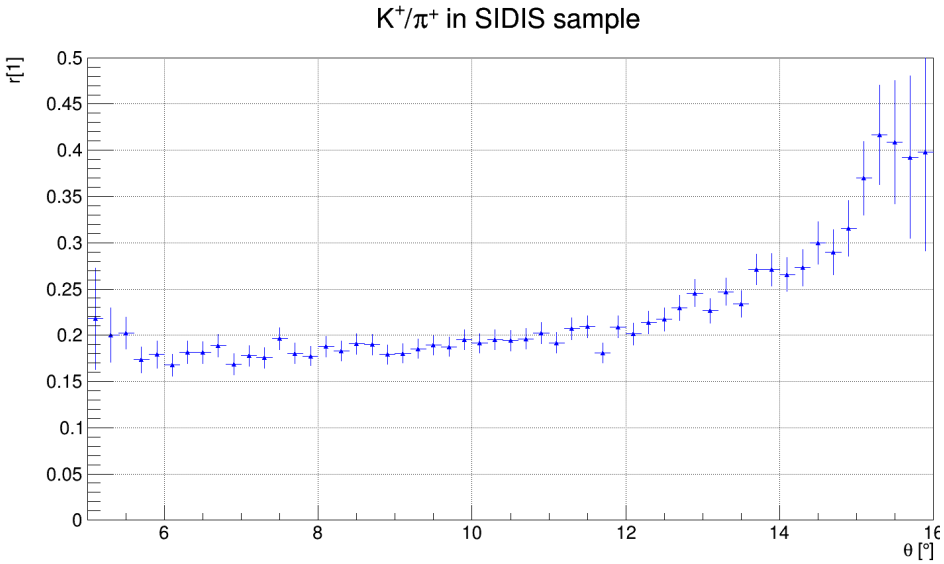

Figure 2.33: Ratio between the pion and kaon distributions as a function of the hadron polar angle.

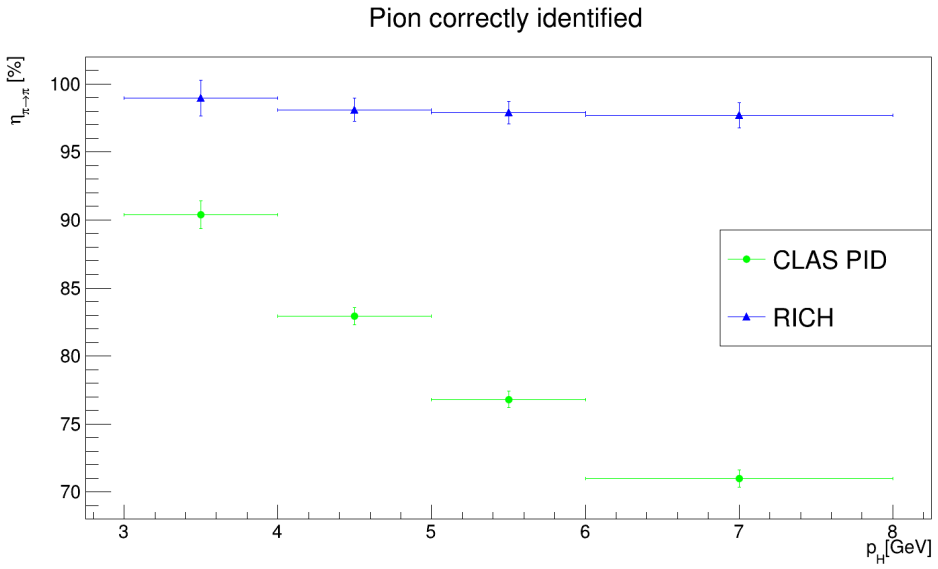

Figure 2.34: Percentage of pion correctly identified over the total of pions passed through the RICH, expressed as a function of the hadron momentum. The results for RICH are obtained by applying the *RQ* cut.

RQ cut is

$$\eta_{\pi\to\pi}^{RICH}(3\,\text{GeV} < p_H < 8\,\text{GeV}) = (97.9 \pm 0.5)\%. \tag{2.11}$$

The percentage of the correctly identified pions was also quantified as a function of the momentum, the comparison with CLAS12 PID performance is shown in Figure 2.34. It shows that the RICH percentage of ~~pion's well identification~~ slightly decreases when the momentum grows, as can be expected because the Cherenkov angle of the ~~two~~ particles became ~~more similar~~. The CLAS12 PID instead quickly decreases when the momentum grows.

Summary and perspective

The Chapter described the CLAS12 RICH, including the general design of this innovative hybrid-optics detector, the assembly of the second module, and the first study on the capability to provide a clean sample of kaons for SIDIS studies. The study presented in the last Section did not aim to perform a precise evaluation of the RICH efficiency, but rather a measurement of the pion rejection factor provided by the detector. ~~This was made because of~~ the high contamination of p~~ion~~ in the kaon sample identified by the CLAS12 PID (without the RICH), which originally was not designed to identify high momentum hadrons. As explained in Chapter 1, a precise PID apparatus is essential to perform ~~measurements of SIDIS~~, accessing the QCD with flavor

sensitivity. The results show that the installation of the first RICH module provided to CLAS12 the capability to identify a clean sample of kaons, with only minimal contamination of pions. This was the first step to exploit the CLAS12 world-leading luminosity to perform high precision measurement on TMDs using kaon, complementing the ongoing studies on pion and providing new constraints to theoretical models. The next Chapter will show how the kaon sample can be used to extract a Beam-Spin Asymmetry (BSA), providing a preliminary measurement of the nucleon structure function $F_{LU}^{\sin\phi}$, which is sensitive to the TMDs with enhanced sensitivity to the strange flavor.